Supporting Information

Contrasting Photochemical Activity of Two Sub-layers for Natural 2D Nanoclay with Asymmetric Layer Structure

Denghui Jiang[a,§], Jie Wang[a,b,§], Ruijie Gao[c,d,*], Liangjie Fu[a,b,*], Huaming Yang[a,b,*]

[a] Hunan Key Lab of Mineral Materials and Application, School of Minerals Processing and Bioengineering, Central South University, Changsha 410083, China

[b] Hunan International Joint Lab of Mineral Materials, Central South University, Changsha 410083, China

[c] Engineering Research Center of Nano-Geomaterials of Ministry of Education, China University of Geosciences, Wuhan 430074, China

[d] Faculty of Materials Science and Chemistry, China University of Geosciences, Wuhan 430074, China

[*]Corresponding authors, Email: hmyang@csu.edu.cn (H. Yang), gaoruijie@cug.edu.cn (R. Gao), franch@csu.edu.cn (L. Fu), Fax: 86-731-88710804, Tel.: 86-731-88830549

[§] These authors contributed equally to this work.

RESULTS AND DISCUSSION

1. The Fe doping in Kaol lattice by DFT calculations

The AKaol obtained by acid etching of 600Kaol only has Si–O sub-layers. During the calcination at 600 ºC, the structural hydroxyl groups of Kaol were removed and crystal structure of Si–O and Al–O sub-layers are well maintained. The atomic models for Kaol, 600Kaol, and AKaol samples are shown in Figure S9a. For Kaol sample, the initial structure of kaolinite (Kaol) is taken from our previous works[1-4]. For 600Kaol sample, the dehyrated model is used by removing the surface OH groups on Al-OH sub-layer. For AKaol sample, the Al leached model is used, taken from our previous work[2]. For Fe doped sample, the models are constructed by Fe replacing Al or Si in Al–O octahedron (Fe–Oct) or Si–O tetrahedron (Fe–Tet). Substitution of Al/Si by one Fe ion in p(4×2) units gave a dopant concentration of 3.12%. The most stable configuration was Al^{3+} substituted by Fe^{3+} of high-spin (Table S2) with the lowest formation energy (3.20 eV, U=0 eV). When considering Fe^{3+} doped in tetrahedral site (Si^{4+}), the charge compensation effect should be considered, similar to the case of Fe doping in Al_2O_3[5]. The formation energy of Fe^{3+} substituted Si^{4+} and Al^{3+} substituted by Si^{4+} was 4.45 eV (U=0 eV), while the energy was 6.90 eV (U=0 eV) only Si^{4+} was substituted by Fe^{3+}. The Fe–O bond lengths for tetrahedrally and octahedrally bonded iron were 1.837(3) and 2.091(2) Å[6]. After geometry optimization with full electronic relaxation, the lengths along z-direction were 1.955 and 2.034 Å (Figure S9b&c and Table S2) in Fe–Tet and Fe–Oct, respectively. Substitution in Si–O sub-layer would arouse significantly greater structural perturbation with an average bond length variety of 0.261 Å (Table S2) and an average Mulliken charge variety of 0.12 e (Table S3). These results further confirmed that Fe–Oct was more stable and the Fe substitution in Al site was easier.

In addition to isomorphous substitution of Fe ion in the lattice, the occupying vacancies within the crystal structures are also considered[7]. We investigated four initial structures with

Fe occupied in the center vacancies of pseudo hexahedral of Kaol. No matter where the initial Fe was, the final Fe in Kaol was in or close to octahedral vacancy (Figure S10). The formation energy in octahedral vacancy was 0.13 eV (U=0 eV) lower than the most unstable structure with Fe in the center of Si, and the results were confirmed with the bond distribution (Figure S10). Partial Al–O bonds were influenced in all the structures, while only individual Si–O bond with strong covalent was severely damaged when Fe occupied in tetrahedral (Figure S11). Owing to the strong combination of Si–O bond, it was very difficult for Fe to occupy the vacancies of tetrahedral stably. The occupying of Fe in octahedral vacancy was steadier than that in tetrahedral. That is to say, whether Fe replaced Al/Si or occupied the vacancies within the crystal structures, the doping was more likely to occur in Al–O sub-layer. But it should be noted that, Fe occupied in octahedral vacancy contributed little for catalysis with the barely changed electron density (Figure S12). The improvement of catalytic activity is mainly provided by Fe substitution in Al/Si sites of Kaol.

2. Photodegradation mechanism of Kaol NSs for different dyes

An obvious difference of photodegradation performance for different dyes was attributed to the significantly different interactions between the dye molecules and Kaol with negatively charge. The RhB molecules were mainly adsorbed on the surfaces of Kaol NSs by electrostatic interaction, while the absorption between OII or MO and Kaol was dependent on weak hydrogen bonding. [8] The OII molecules are relatively difficult to directly react with photo-generated holes and surface ROS on the surface of Kaol due to electrostatic repulsion, while RhB can. Thus, the photodegradation ability of OII is obvious lower than that of RhB for Fe doped Kaol. The OII molecules are mainly photo-degraded by the ROS of the bulk solution. The direct degradation of RhB by photo-generated holes and surface ROS can explained that the difference of the RhB photodegradation ability of the two sub-layers is less

pronounced than that of OII photodegradation. CIP molecules were strongly absorbed on surfaces of Kaol due to the hydrogen bonding and thus were photo-degraded by Kaol NSs.

Moreover, the Al–O sub-layers has a stronger interaction with the RhB molecules than the Si–O sub-layers, due to stronger negatively charged surfaces caused by more isomorphous substitution of Fe iron, which is supported by the same adsorption capacity of 600Kaol and AKaol for RhB (Figure S3b). Thus, the surface reaction efficiency of RhB on Al–O sub-layers may be higher than that on Si–O sub-layers.

Table S1 Formation energy of Fe substitution in different sites.

Substitute site	Initial electronic configuration of Fe			Subsequent electronic configuration of Fe		Formation energy (eV)
	Hubbard U of Fe (eV)	Formal charge (e)	Formal spin (μB)	Mulliken charge (e)	Mulliken spin (μB)	
Fe→Al	0	+2	4 (HS)	1.49	4.08	3.28
		+3	5 (HS)	1.49	4.08	3.20
		+3	1 (LS)	1.29	0	3.27
	3.5	+3	5 (HS)	1.54	4.20	4.69
Fe→Si	0	+2	4 (HS)	1.33	0	6.93
		+3	5 (HS)	1.33	0	6.90
		+3	1 (LS)	1.33	0	6.90
Fe→Si	0	+3	5 (HS)	1.45	3.98	4.45
Si→Al	3.5	+3	5 (HS)	1.51	4.10	6.18

Table S2 DFT-calculated interatomic distances (Å) and bond populations of Kaol before and after Fe substituted in different sites.

Substitution site	Bond	Before substitution		After substitution		Variety	
		Population	Length (Å)	Population	Length (Å)	Population	Length (Å)
Al–O Octahedron	Al–O1	0.29	1.931	0.22	2.044	-0.07	0.113
	Al–O2	0.29	1.918	0.21	2.038	-0.08	0.120
	Al–O3	0.30	1.891	0.22	1.998	-0.08	0.107
	Al–O4	0.30	1.917	0.20	2.034	-0.10	0.117
	Al–O5	0.29	1.911	0.21	2.033	-0.08	0.122
	Al–O6	0.29	1.954	0.22	2.057	-0.07	0.103
	Average	0.29	1.920	0.21	2.034	-0.08	0.114
Si–O Tetrahedron	Si–O1	0.54	1.619	0.32	1.871	-0.22	0.251
	Si–O2	0.57	1.640	0.28	1.955	-0.29	0.315
	Si–O3	0.54	1.614	0.35	1.845	-0.19	0.231
	Si–O4	0.52	1.616	0.34	1.861	-0.18	0.245
	Average	0.54	1.622	0.32	1.883	-0.22	0.261

Table S3 DFT-calculated atom Mulliken charges of Kaol before and after Fe substituted in different sites.

Substitution site	Atom	Before substitution (e)	After substitution (e)	Variety(e)
Al–O Octahedral	O1	-1.15	-1.09	0.06
	O2	-1.05	-0.97	0.08
	O3	-1.03	-0.95	0.08
	O4	-1.05	-0.97	0.08
	O5	-1.05	-0.97	0.08
	O6	-1.15	-1.09	0.06
	Average	-1.08	-1.01	0.07
Si–O Tetrahedral	O1	-1.16	-1.03	0.13
	O2	-1.15	-1.06	0.09
	O3	-1.16	-1.03	0.13
	O4	-1.17	-1.05	0.12
	Average	-1.16	-1.04	0.12

Table S4 Data fitting using a Langmuir-Hinshelwood model and reaction rate constant for photo-degradation of RhB, OII and CIP in the presence of different samples

Samples	K^a	Standard Error	R^2
Kaol	0.0122	0.0012	0.9725
300Kaol	0.0275	0.0010	0.9960
500Kaol	0.0343	0.0018	0.9919
600Kaol	0.0317	0.0005	0.9993
AKaol	0.0375	0.0049	0.9509
600AKaol	0.0314	0.0057	0.9084
WKaol	0.0139	0.0030	0.9981
600WKaol	0.0320	0.0027	0.9785
Kaol(OII)	0.0023	$4.6*10^{-4}$	0.9985
600Kaol(OII)	0.0019	$5.3*10^{-4}$	0.7471
AKaol(OII)	0.0002	$1.1*10^{-4}$	0.4129
600Kaol(CIP)	0.0012	$1.1*10^{-4}$	0.9535
AKaol(CIP)	0.0006	$1.0*10^{-4}$	0.8446

[a] The K was calculated from the first 30 min data for the RhB degradation data, 120 and 150 min data for the OII and CIP degradation data.
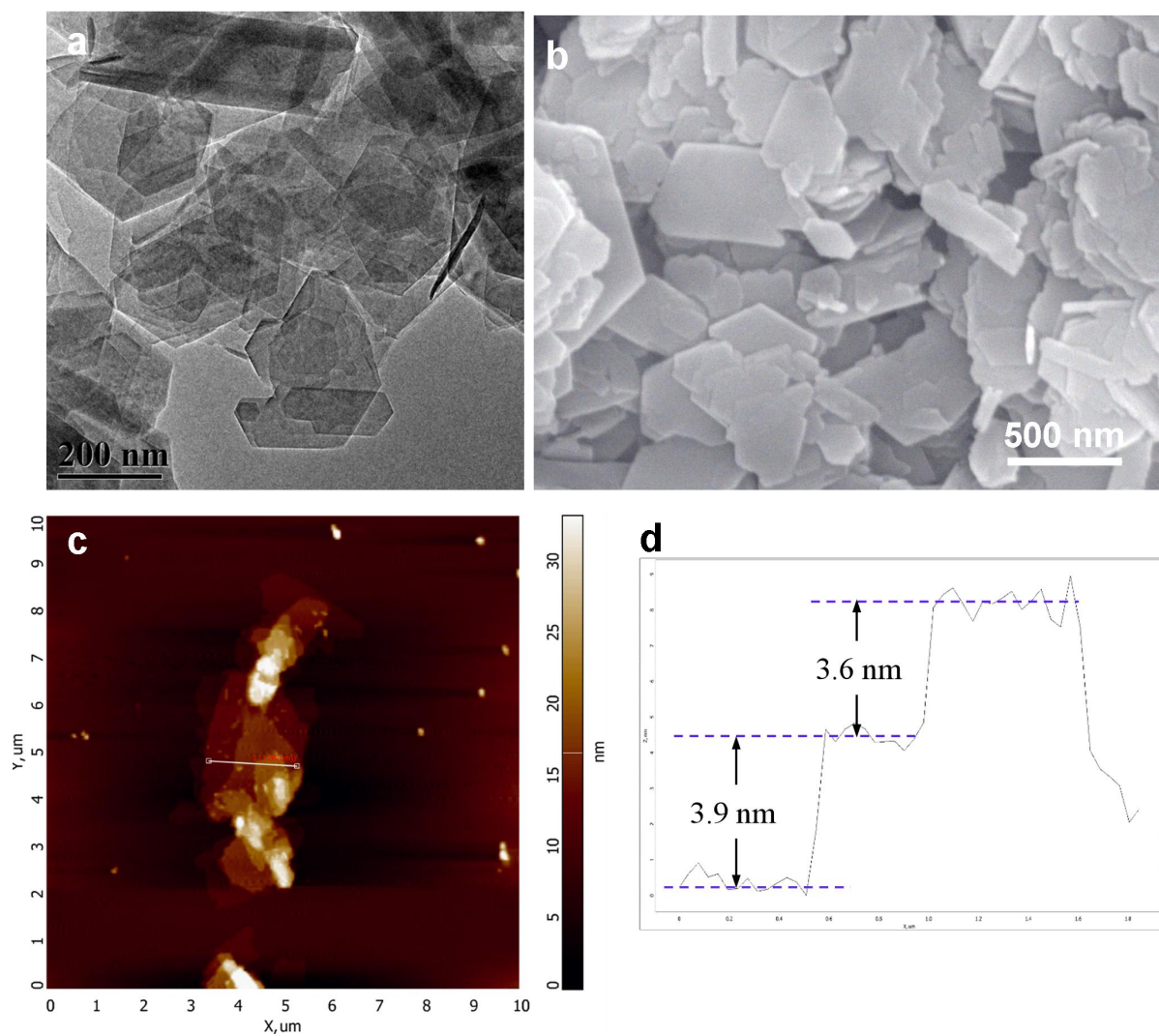
Figure S1. (a) TEM, (b) SEM, (c) AFM images and (d) height profile of Kaol NSs
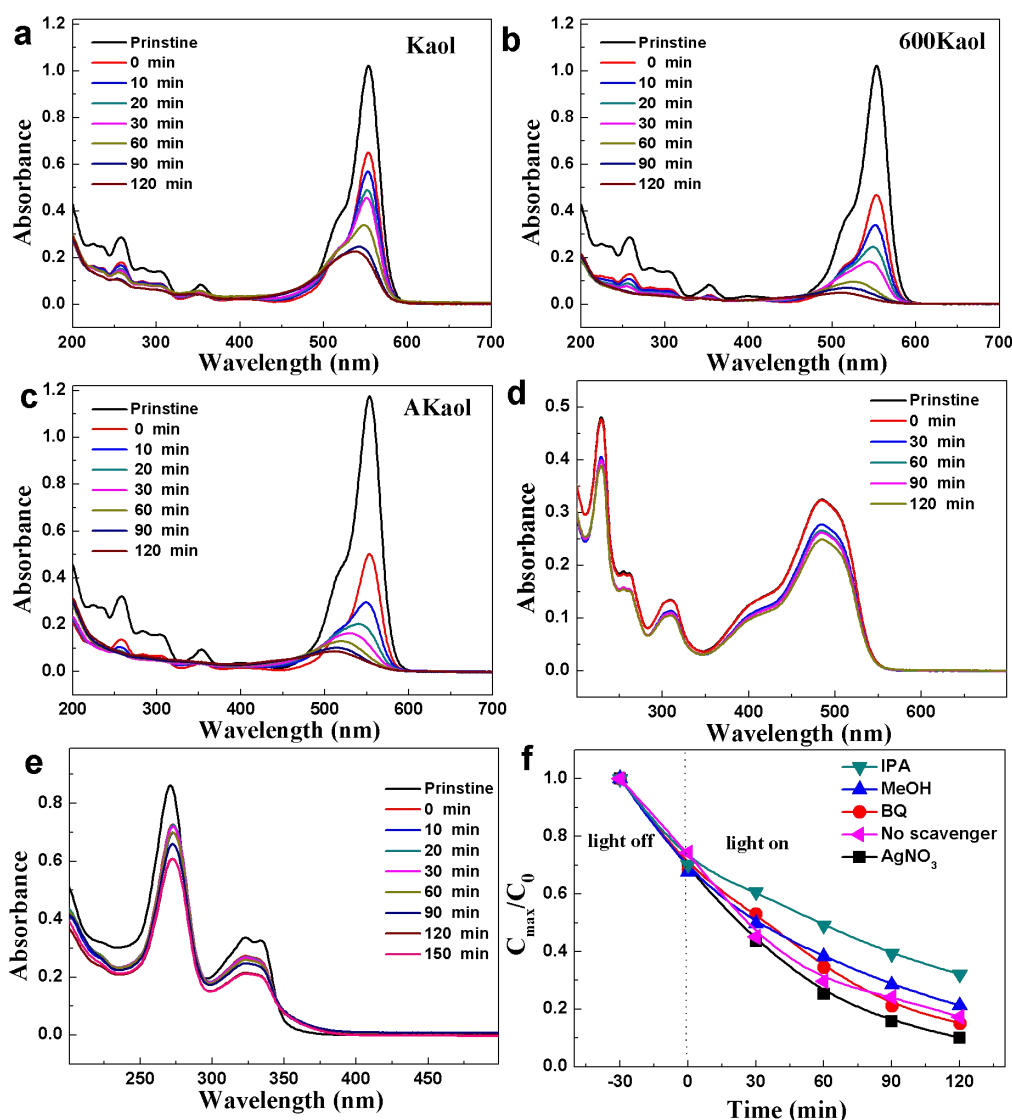
Figure S2. Time-dependent absorption spectra of RhB photodegradation in present of (a) Kaol, (b) 600Kaol and (c) AKaol samples. Time-dependent absorption spectra of (d) OII and (e) CIP photodegradation in present of 600Kaol. (It should be noted that the raw Kaol almost completely adsorbed CIP, we only compared the photodegradation ability of 600Kaol and AKaol samples). (f) Active species trapping experiments of Kaol NSs, 0.54 mg of BQ, 8.5 mg of AgNO$_3$, 1.6 g of MeOH and 3 g of IPA were added in the photodegradation reaction, respectively.

In the active species trapping experiments (Figure S2f), the accelerated the photodegradation rate induced by addition of AgNO$_3$ implied the serious recombination of photo-generated electrons, which resulted from the poor conductivity of aluminosilicate framework. Thus, we inferred that only the photo-generated holes on the outermost surface of Kaol efficiently generated •OH radicals and reacted with the dye molecules.[9] These findings suggest that the dye photodegradation of Kaol NSs strongly depends on its surfaces.
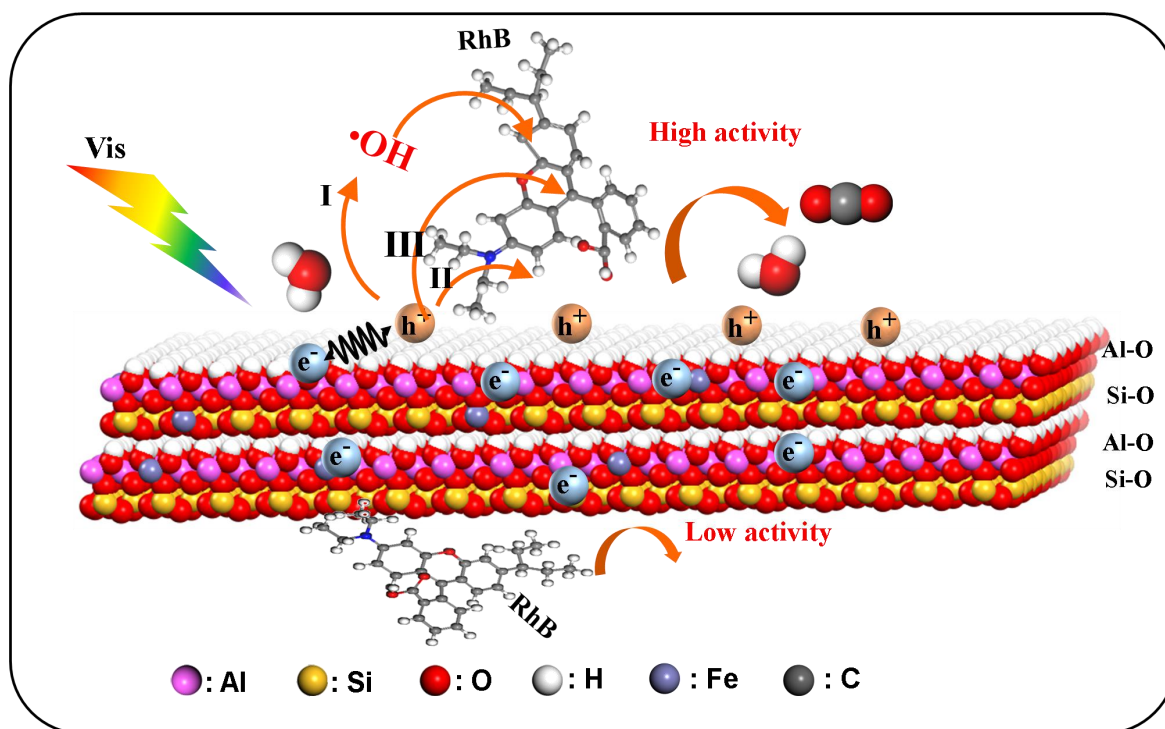
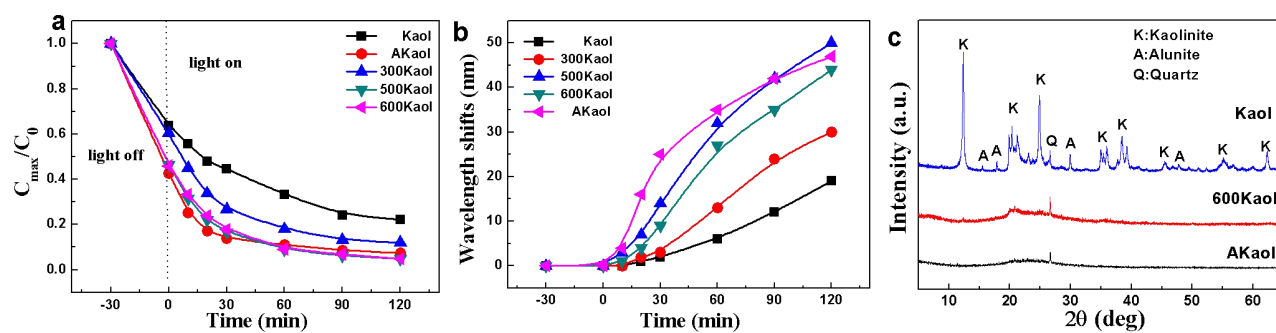**Figure S3.** Proposed mechanism of Kaol NSs for RhB photodegradation

Figure S4. (a) Photodegradation curves of TKaol and AKaol for RhB photodegradation. (b) Wavelength shifts of the time-dependent absorption spectra in present of different samples. (c) XRD patterns of different samples
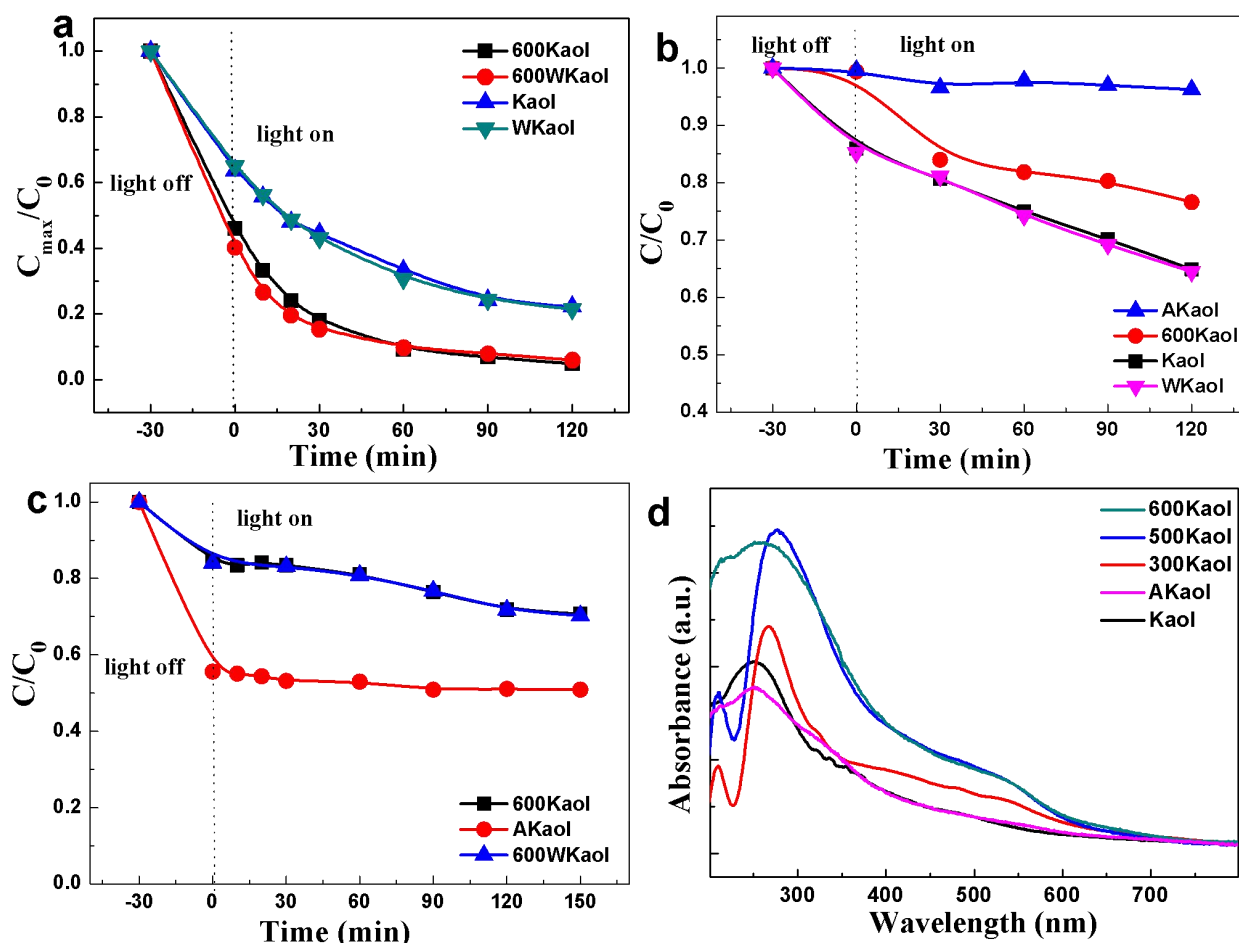
Figure S5. Photodegradation curves of Kaol, 600Kaol, WKaol, 600WKaol and AKaol for the photodegradation of (a) RhB, (b) OII and (c) CIP. (The WKaol sample almost completely adsorbed CIP, thus we compared the photodegradation ability of 600Kaol and 600WKaol samples to investigate the effect of free Fe ions on the photocatalytic performance of Kaol NSs for CIP photodegradation). (d) UV-vis diffuse reflection spectrum of different samples.

The reduced band gap of Fe doped Kaol nanoclay leads to the enhanced visible light absorption.[10] As shown in Fig. S5d, the strong absorption peaks at ca. 210 nm and 250 nm were corresponded to interband transitions. The absorption band in the region of 300~400 nm is attributed to ligand-metal charge transfer. The absorption bands at 550 nm were assigned to the intraband d-d transitions.[6]
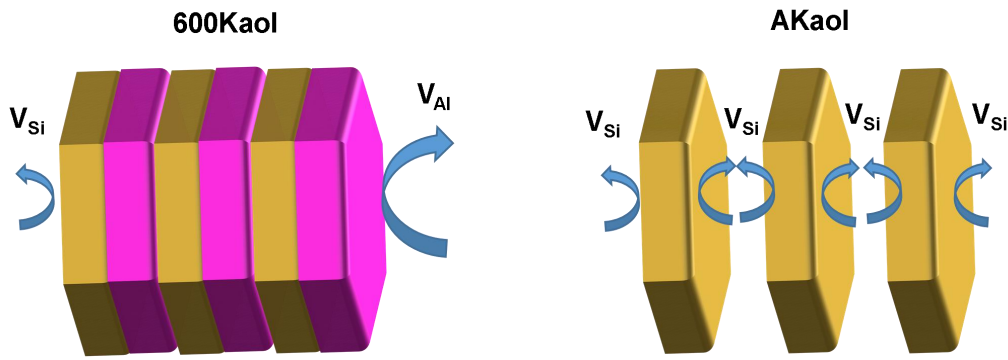
Figure S6. Schematic structure of 600Kaol and AKaol.

Photodegradation reactions are difficult to occur between lamellae of Kaol due to the small layer spacing.[11] On the other hand, the enlarged layer spacing of the AKaol greatly increased specific surface area and facilitate the reaction of photogenerated holes with water and dyes molecules. Generally, the apparent photocatalytic rate (K) of photocatalysts is proportional to the photodegradation ability (V) and specific surface area (S). The photodegradation ability was expressed as the photocatalytic reaction rate normalized by specific surface area:

$$V = K/S \tag{1}$$

Both Al–O and Si–O sub-layers account for half of the specific surface area of 600Kaol. Thus, the apparent photocatalytic rate of 600Kaol can be expressed as:

$$K_{600Kaol} = V_{Al} * \frac{S_{600Kaol}}{2} + V_{Si} * \frac{S_{600Kaol}}{2} = S_{600Kaol} * (V_{Al} + V_{Si})/2 \tag{2}$$

$$V_{600Kaol} = (V_{Al} + V_{Si})/2 \tag{3}$$

$$\text{Thus, } V_{Al} = 2V_{600Kaol} - V_{Si} \tag{4}$$

where V_{Al} and V_{Si} are photodegradation ability of Al–O and Si–O sub-layers of Kaol, respectively. The photocatalytic degradation ability of the Si–O sub-layers of Kaol was replaced by that of the AKaol. The ratio of photodegradation ability for Al–O and Si–O sub-layers showed as follow:

$$\frac{V_{Al}}{V_{Si}} = \frac{2V_{600Kaol}}{V_{AKaol}} - 1 \tag{5}$$
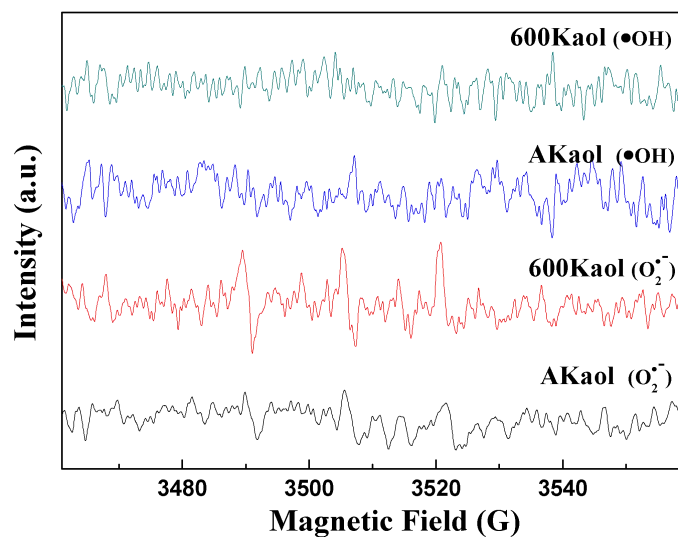
Figure S7. ESR spectra of DMPO-•OH obtained from the 600Kaol and AKaol samples in dark.

EPR spectra of all samples exhibited obvious hydroxyl radicals (•OH) and superoxide radicals (O_2•$^-$) signals (Figure 3d), whereas almost no clear radicals signal was observed in the dark, indicating the obvious photochemical activity of Fe doped Kaol NSs under visible-light irradiation.
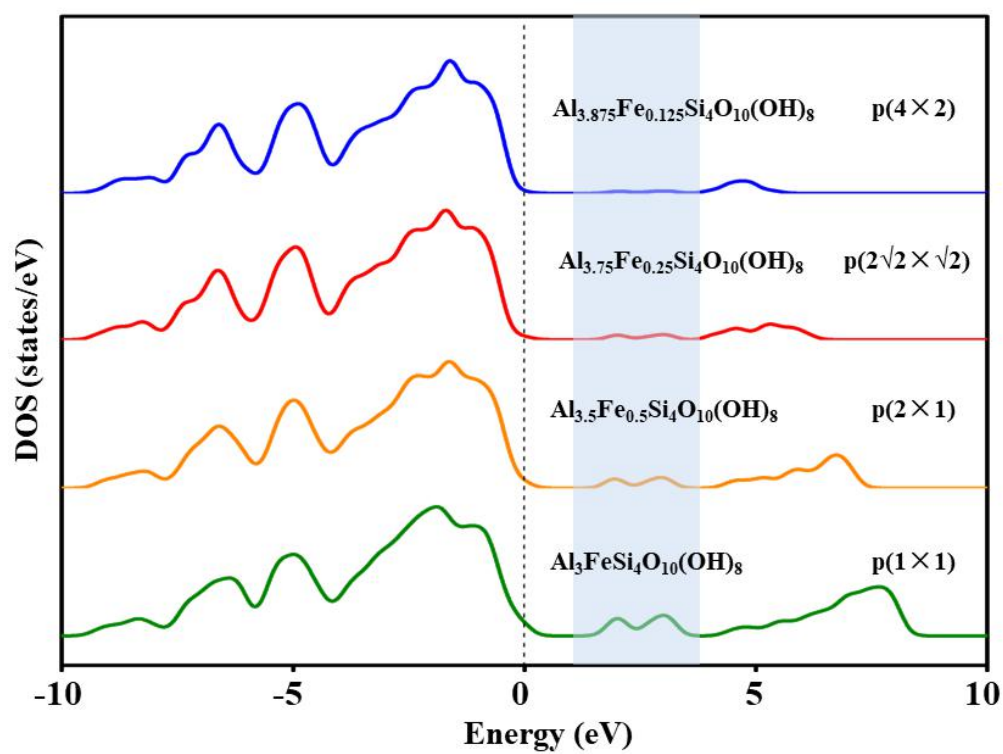
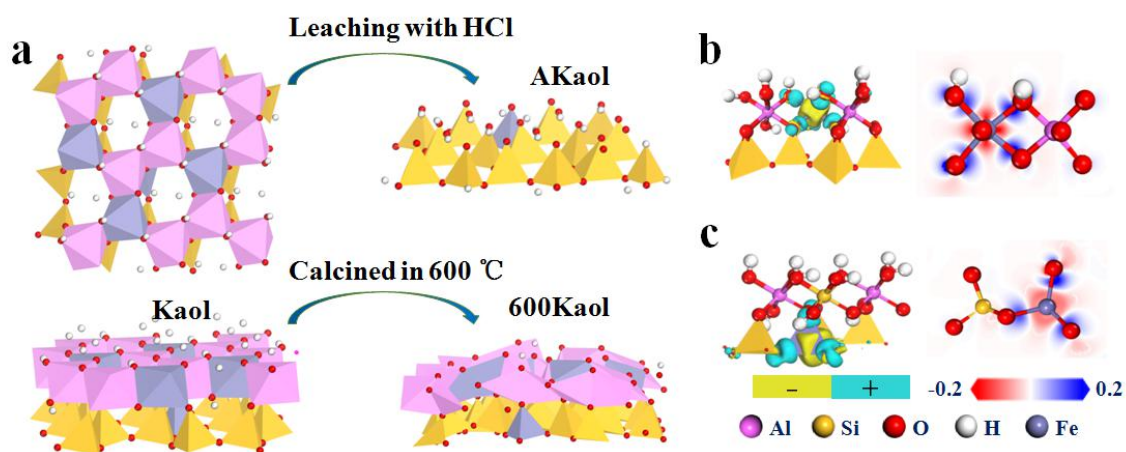**Figure S8.** DOS of Fe–Oct with different concentrations of Fe.

Figure S9. (a) Models for Kaol, 600Kaol and AKaol with Fe impurities. Density difference of Fe doped Kaol in (b) octahedron and in (c) tetrahedron. The isovalue are 0.04 e/Å^3.

The Fe–O bond lengths for tetrahedrally and octahedrally bonded iron were 1.837(3) and 2.091(2)Å [6], while the lengths along the Z direction after optimization were 1.955 and 2.034 Å (Figure S1) in Fe–Tet and Fe–Oct, respectively. Lattice optimization and electrostatic effects induced by charge transfers could affected the energy levels.[12-13]
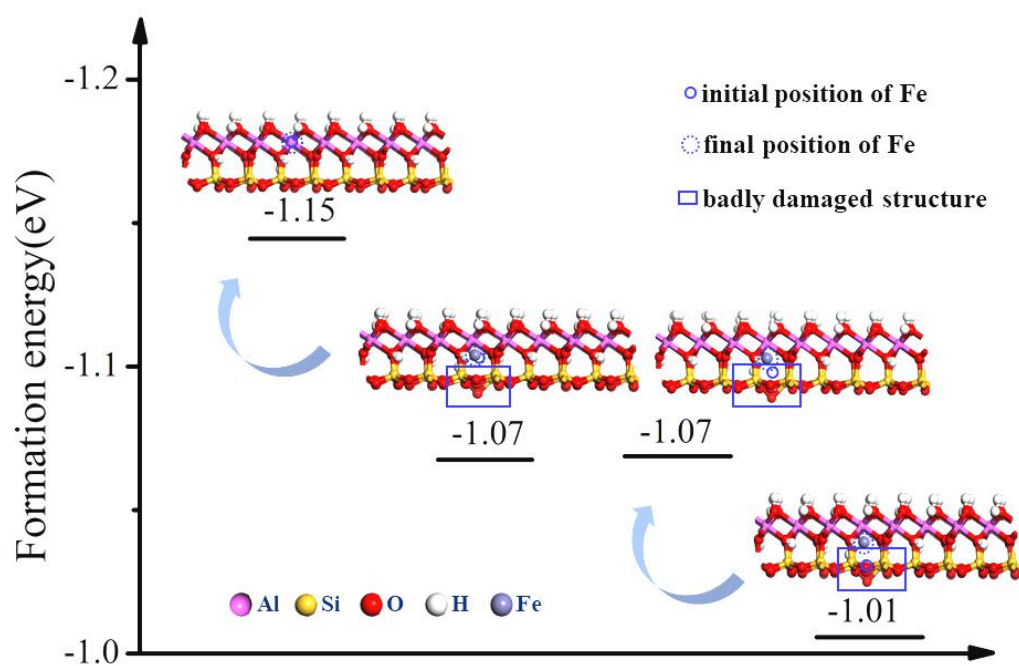
Figure S10. Formation energy and final structures of Kaol with Fe occupied in octahedral and tetrahedral vacancies.
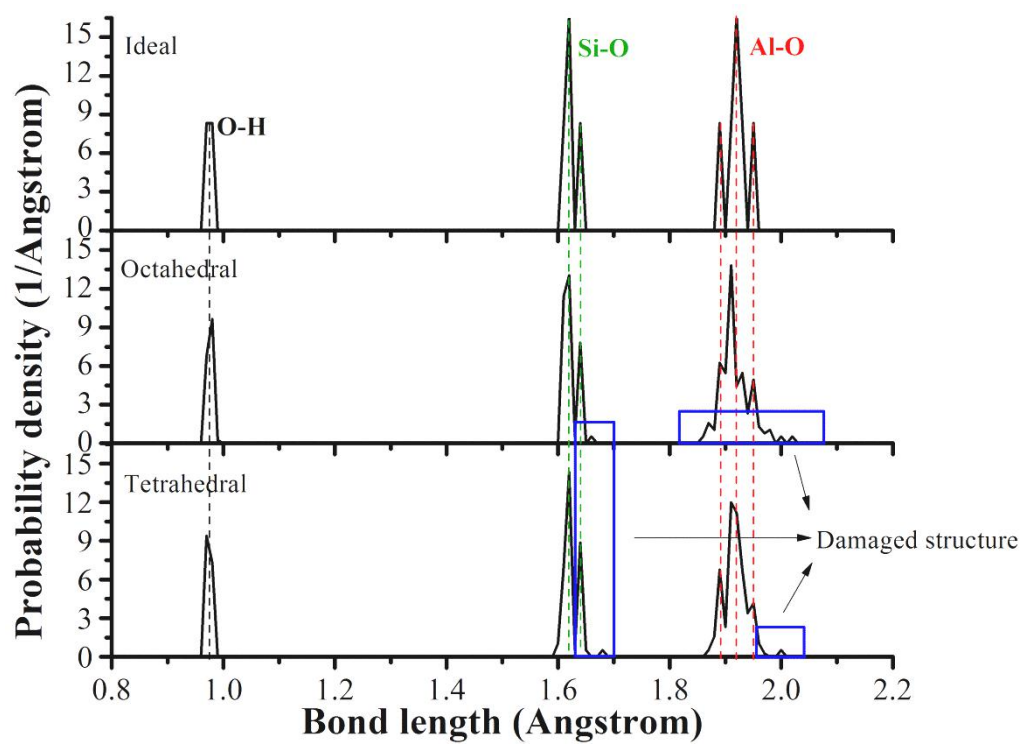
Figure S11. Probability density of bond length of ideal Kaol and Kaol with Fe occupied in octahedral and tetrahedral vacancies.
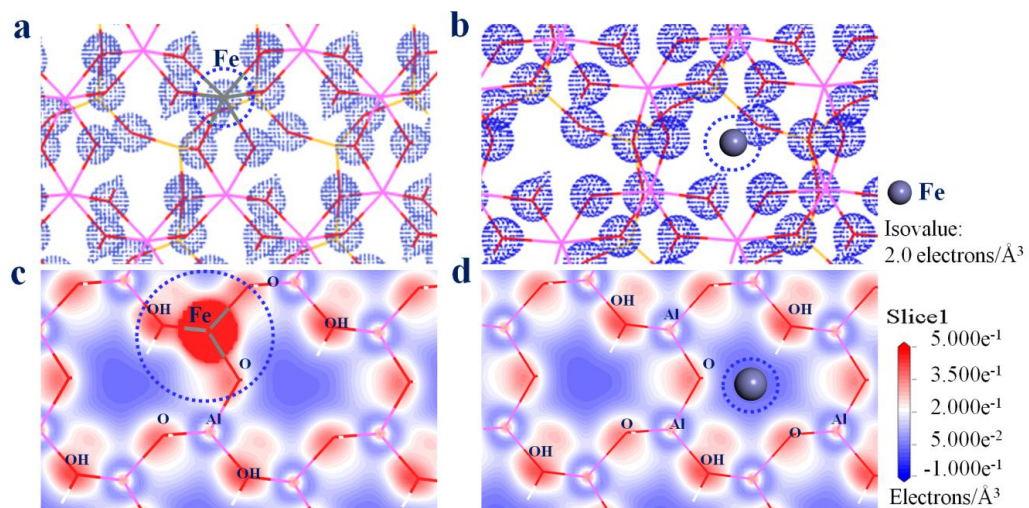
Figure S12. Electron density maps of Fe substituted octahedral site (a, c) and Fe occupied in octahedral vacancy (b, d).

REFERENCES

(1) Zhao, Q.; Fu, L.; Jiang, D.; Ouyang, J.; Hu, Y.; Yang, H.; Xi, Y., Nanoclay-Modulated Oxygen Vacancies of Metal Oxide. *Communications Chemistry* **2019,** *2*, 11.

(2) Fu, L.; Yang, H.; Tang, A.; Hu, Y., Engineering a Tubular Mesoporous Silica Nanocontainer with Well-Preserved Clay Shell from Natural Halloysite. *Nano Research* **2017,** *10*, 2782-2799.

(3) Zhang, Y.; Fu, L.; Shu, Z.; Yang, H.; Tang, A.; Jiang, T., Substitutional Doping for Aluminosilicate Mineral and Superior Water Splitting Performance. *Nanoscale Research Letters* **2017,** *12*, 456.

(4) Fu, L.; Yang, H., Structure and Electronic Properties of Transition Metal Doped Kaolinite Nanoclay. *Nanoscale Research Letters* **2017,** *12*, 411.

(5) Fu, L.; Yang, H.; Hu, Y.; Wu, D.; Navrotsky, A., Tailoring Mesoporous γ-Al$_2$O$_3$ Properties by Transition Metal Doping: A Combined Experimental and Computational Study. *Chemistry of Materials* **2017,** *29*, 1338-1349.

(6) Jørgensen, J.-E.; Mosegaard, L.; Thomsen, L. E.; Jensen, T. R.; Hanson, J. C., Formation of γ-Fe$_2$O$_3$ Nanoparticles and Vacancy Ordering: An in Situ X-ray Powder Diffraction Study. *Journal of Solid State Chemistry* **2007,** *180*, 180-185.

(7) Ceylantekin, R.; Başar, R., Solid Solution Limit of Fe$_2$O$_3$ in Mullite Crystals, Produced from Kaolin by Solid State Reactions. *Ceramics International* **2018,** *44*, 7599-7604.

(8) Chen, H.; Zhong, A.; Wu, J.; Zhao, J.; Yan, H., Adsorption Behaviors and Mechanisms of Methyl Orange on Heat-Treated Palygorskite Clays. *Industrial & Engineering Chemistry Research* **2012,** *51*, 14026-14036.

(9) Nosaka, Y.; Nosaka, A., Understanding Hydroxyl Radical (•OH) Generation Processes in Photocatalysis. *ACS Energy Letters* **2016,** *1*, 356-359.

(10) Jiang, D.; Liu, Z.; Fu, L.; Jing, H.; Yang, H., Efficient Nanoclay-Based Composite Photocatalyst: The Role of Nanoclay in Photogenerated Charge Separation. *The Journal of Physical Chemistry C* **2018,** *122*, 25900-25908.

(11) Liu, Q.; Li, X.; Cheng, H., Insight into the Self-Adaptive Deformation of Kaolinite Layers into Nanoscrolls. *Applied Clay Science* **2016,** *124-125*, 175-182.

(12) Kim, J.; Chung, C.-H.; Hong, K.-H., Understanding of the Formation of Shallow Level Defects from the Intrinsic Defects of Lead Tri-Halide Perovskites. *Physical Chemistry Chemical Physics* **2016,** *18*, 27143-27147.

(13) Li, J.; Yang, J.; Wu, T.; Wei, S., Formation of DY Center as N-Type Limiting Defects in Octahedral Semiconductors: the Case of Bi-Doped Hybrid Halide Perovskites. *Journal of Materials Chemistry C* **2019,** *7*, 4230-4234.